Harmonic-Domain SISO Equivalent Impedance Modeling and Stability Analysis of a Single-Phase Grid-Connected VSC

Chen Zhang, Marta Molinas, *Member, IEEE*, Sjur Føyen, *Member, IEEE*, Jon Are Suul, *Member, IEEE*, and Takanori Isobe, *Member, IEEE*

***Abstract*—This article presents a harmonic-domain single-input single-output (SISO) equivalent modeling technique for the impedance modeling and stability analysis of a single-phase grid-connected voltage-source converter (VSC). The basis is a conversion technique that transforms a harmonic transfer function (HTF)-based model into a SISO equivalent model while preserving all the information of frequency couplings. The proposed SISO modeling concept is useful for understanding the meaning and consequence of SISO impedance measurement of an interconnected system with frequency couplings, which further enables a simpler impedance measurement and impedance-based analysis. Applications of this method for the VSC model reduction and stability characteristic analyses are presented. From these results, useful conclusions regarding the accuracy of three types of reduced-order VSC impedance models and the stability effects of the VSC control with and without compensation for dc voltage variation are obtained. The presented examples of applications demonstrate how the proposed SISO modeling technique facilitates a simpler and efficient impedance-based analysis. Finally, experimental results verify the validity of the proposed VSC-SISO admittance and corresponding analyses.**

***Index Terms*—Impedance, Nyquist, single-input single-output (SISO), stability, voltage-source converter (VSC).**

I. Introduction

VOLTAGE-SOURCE converters (VSCs) are being commonly utilized in electrical systems due to their flexibility and controllability. Common applications include grid integration of wind/photovoltaic power generation [1], interconnection of ac systems through the high-voltage dc (HVdc) transmissions [2], electric drive systems for locomotives [3], etc. With the increasing penetration of VSCs in power systems, interactions among the VSCs and the grid can lead to small-signal instability, e.g., the oscillatory phenomenon discussed in [4] and [5]. Thus, it is necessary to analyze the small-signal behavior of VSCs and its consequences on stability. In this respect, the impedance-based method can be applied and is gaining popularity since the impedance of the VSC can be readily derived either from analytical modeling or measurement [6]–[9].

In terms of the impedance modeling, there are two main methods: the linear time-invariant (LTI)-framework-based, and the linear time-periodic (LTP)-framework-based methods [7]. The former one usually applies to VSCs whose linearized models can be represented as LTI systems via transformations (e.g., *dq*-transformation). Therefore, corresponding impedance models can be readily obtained in the Laplace domain or the complex domain [8]. Impedance modeling of a three-phase VSC by such methods is, for instance, discussed in [9]–[11]. On the other hand, if such an equivalent LTI model is unachievable, then the impedance modeling has to be conducted directly on the original linearized system that is an LTP system in general. In this regard, the harmonic linearization method based on the principle of harmonic balance [12] can be adopted. Applications of this method in deriving the impedances of a single-phase VSC, a three-phase VSC, and a modular multilevel converter (MMC) [13] are presented in [14], [15], and [16] respectively.

Recent analyses have shown that VSCs generally exhibit frequency coupling behavior and the number of coupled frequencies depends on the studied topology. For example, the number of frequency couplings in a three-phase VSC is typically bounded by two [17]–[19], which is interpreted as the mirror frequency coupling (MFC) effect in [19]. For a single-phase VSC, the number of coupled frequencies is conceptually infinite [16], due to the time-periodic nature of the system. It is also usually cumbersome to apply the harmonic linearization method to obtain the VSC impedance exhibiting a large number of frequency couplings. Instead, the LTP-framework-based methods, e.g., harmonic state space (HSS) [20] or the harmonic transfer function (HTF) [21] methods, are more feasible for the impedance modeling of such systems. This is because the process of transforming an LTP system from time- to frequency-domain is well defined and the frequency couplings are inherently accounted in that process. Examples of applying the HSS in the harmonic stability analysis of a single-phase VSC and an MMC are for instance presented in [22]–[25]. Besides, it is noticed that although this HSS/HTF method can model

Manuscript received May 19, 2019; revised August 26, 2019 and December 2, 2019; accepted January 21, 2020. Date of publication January 31, 2020; date of current version May 1, 2020. This work was supported by Norwegian University of Science and Technology (NTNU) under the Grant NTNU Energy (81617922). Recommended for publication by Associate Editor J. Liu. *(Corresponding author: Chen Zhang.)*

C. Zhang and M. Molinas are with the Department of Engineering Cybernetics, Norwegian University of Science and Technology, Trondheim 7034, Norway (e-mail: chen.zhang@ntnu.no; marta.molinas@ntnu.no).

S. Føyen is with the Department of Electric Power Engineering, NTNU, Trondheim 7034, Norway (e-mail: foyen.sjur@ntnu.no).

J. A. Suul is with SINTEF Energy Research, Trondheim 7491, Norway, and also with the Department of Engineering Cybernetics, Norwegian University of Science and Technology, Trondheim 7034, Norway (e-mail: jon.a.suul@sintef.no).

T. Isobe is with the Faculty of Pure and Applied Sciences, University of Tsukuba, Ibaraki 305-8573, Japan (e-mail: isobe.takanori.gf@u.tsukuba.ac.jp).

Color versions of one or more of the figures in this article are available online at https://ieeexplore.ieee.org.

Digital Object Identifier 10.1109/TPEL.2020.2970390

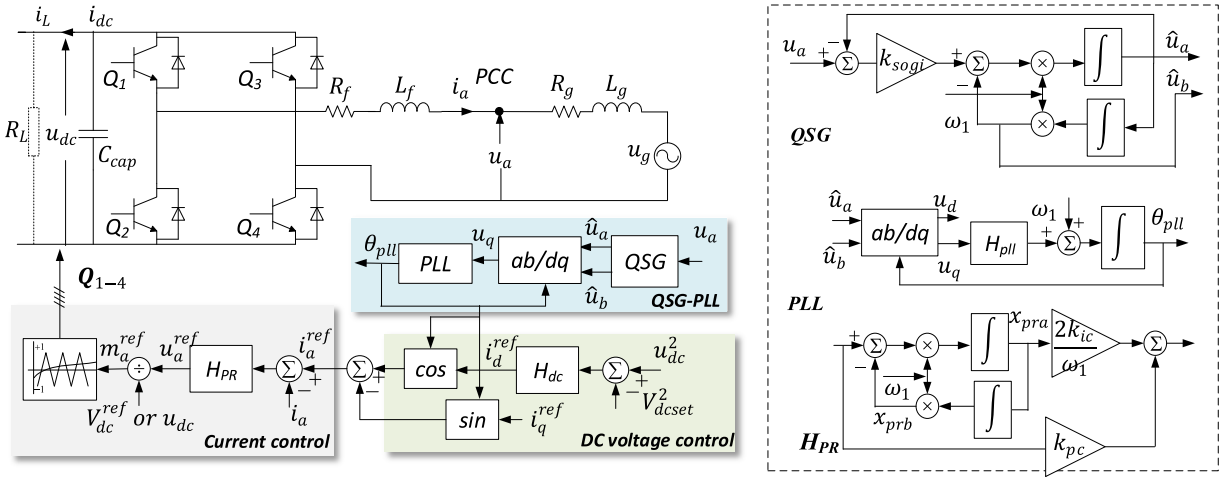

Fig. 1. Schematic of a typical single-phase grid-VSC system. (a) Main circuit and control strategy. (b) Control blocks.

an LTP system and the frequency characteristic systematically, the resulting impedance is usually a large dimensional matrix representing a multi-input multioutput (MIMO) system. This brings significant challenges in impedance measurement and impedance-based analysis, which motivates model simplifications, for example, by excluding the frequency components that are insignificant for impedance modeling.

Relevant analyses with respect to the single-phase VSCs are introduced in [26]–[28], in which, the development of these impedance models is commonly based on the assumption that the steady-state harmonics in the system are negligible. This simplification brings two effects: the number of frequency couplings for impedance modeling is drastically reduced, and the approximate system becomes LTI so that the conventional time- to frequency-domain transformation can be applied for impedance extraction. Based on a similar assumption, Zhang *et al*. [14] and Shah and Parsa [29] developed the sequence impedance of a single-phase VSC by means of harmonic linearization. Basically, the abovementioned impedance models regardless of modeling domains are characterized by a 2-by-2 matrix that can primarily capture the MFC effect with the single-phase VSC system. A latest work by Qian *et al.* [30] extends the model into a 3-by-3 matrix being able to capture more frequency components so that the model accuracy is improved. It can be obtained that the more frequency components considered in the modeling process, the more accurate the resulting model. However, it lacks a model comparison and a clarification on how many frequency components should be considered for modeling. To fulfill such requirements, or more generally, to facilitate better impedance-based analyses, the MIMO impedance obtained from the HSS/HTF is not a desirable choice, and thus it would be of significant importance to develop a simple and high-fidelity model that can simplify the impedance-based analysis.

To fill this gap, this article presents a single-input single-output (SISO) equivalent modeling technique for the impedance modeling and analysis of the single-phase grid-connected VSC. Based on this SISO modeling technique, this article further clarifies the accuracy of several reduced-order VSC impedance models obtained from different truncations of the HTF-based model and discusses the stability impacts of the VSC controls with and without compensation of the dc voltage variation. These studies also demonstrate how the proposed SISO modeling technique facilitates a simpler and more practically applicable impedance-based analysis.

II. Harmonic-Domain Impedance Modeling and Analysis of the Single-Phase Grid-VSC System

A. Study System

Fig. 1 depicts a typical single-phase grid-VSC system composed of a full-bridge VSC, an *L*-type filter, a resistive dc load, and a Thevenin equivalent grid. The outer-loop controls the average value of the squared dc voltage using a proportional–integral regulator, whereas the inner-loop controls the ac current using a proportional–resonant (PR) regulator. The grid synchronization is fulfilled by a quadrature signal generator (QSG) based on a second-order generalized integrator (SOGI) and a conventional phase-locked loop (PLL).

As also indicated in the lower left of Fig. 1, two approaches for calculating the modulation index m_a^{ref} are considered

$$\begin{cases} m_a^{\mathrm{DM}} = u_a^{\mathrm{ref}}/V_{\mathrm{dc}}^{\mathrm{ref}} \\ m_a^{\mathrm{CM}} = u_a^{\mathrm{ref}}/u_{\mathrm{dc}} \end{cases} \tag{1}$$

where $m_{\mathrm{a}}^{\mathrm{DM}}$ obtained with a constant dc voltage $V_{\mathrm{dc}}^{\mathrm{ref}}$ is referred to as the direct modulation (DM) case in this article; and $m_{\mathrm{a}}^{\mathrm{CM}}$obtained with an instantaneous dc voltage u_{dc} is referred to as the compensated modulation (CM) case. In addition, the CM usually results in better power quality than the DM [31]. In this article, the CM and DM cases are used mainly because they represent two different operating conditions for steady-state harmonics without introducing too many differences in the control system. Thus, they are useful examples not only for illustrating the application of the proposed SISO equivalent modeling, but also for evaluating the impacts of steady-state harmonics on the extent of frequency couplings, model reduction, and small-signal stability.

B. Modeling Conventions

For an LTI element, e.g., the dc voltage controller $H_{\mathrm{dc}}(s) = k_{\mathrm{pdc}} + \frac{k_{\mathrm{idc}}}{s}$, its harmonic-domain model (i.e., the

HTF) is composed of the frequency-shifted copies of $H_{\mathrm{dc}}(s)$ [21]

$$H_{\mathrm{dc}}(s) = \mathrm{diag}(\cdots, H_{\mathrm{dc}}(s - j\omega_1), H_{\mathrm{dc}}(s), H_{\mathrm{dc}}(s + j\omega_1), \cdots). \quad (2)$$

For brevity, in the later analysis, the notation $H_{\mathrm{dc}(k)}(s)$ will be adopted for representing the component $H_{\mathrm{dc}}(s + k \cdot j\omega_1)$, and the Laplace variable in $H_{\mathrm{dc}(k)}(s)$ is often omitted.

For an LTP element, such as $A(t)$, its harmonic-domain model is a Toeplitz matrix [20] ($P\{\}$ is the Toeplitz operator)

$$P\{A(t)\} = \begin{bmatrix} \ddots & \ddots & \ddots & & \\ \ddots & A_0 & A_{-1} & A_{-2} & \\ \ddots & A_{+1} & A_0 & A_{-1} & \ddots \\ & A_{+2} & A_{+1} & A_0 & \ddots \\ & & \ddots & \ddots & \ddots \end{bmatrix} \quad (3)$$

in which $A_{\pm k}$ is the $\pm k$th Fourier coefficient of A(t).

In general, the harmonic-domain models of the VSC and grid are derived according to the following steps:

1) perform the linearization on system blocks;
2) transform the linearized blocks into the harmonic domain;
3) formulate the harmonic-domain impedance/admittance using the transformed blocks in conjunction with circuit and control diagrams.

In later analysis, these steps are applied without any further detailed discussions.

C. Harmonic-Domain Models of the Grid-VSC System

1) VSC Harmonic-Domain Admittance: Based on the above-mentioned modeling process, the VSC harmonic-domain admittance defined as

$$-\Delta \boldsymbol{I}_a(s) = \boldsymbol{Y}_c^{\mathrm{HTF}}(s) \cdot \Delta \boldsymbol{U}_a(s) \quad (4)$$

can be derived, where $\boldsymbol{Y}_c^{\mathrm{HTF}}(s)$ is given in (5). By setting the parameters $\boldsymbol{K}_1$ and $\boldsymbol{K}_2$ in (5), shown at the bottom of this page, to one of the following combinations:

$$\mathrm{CM}: \boldsymbol{K}_1 = \boldsymbol{U}_{\mathrm{dc0}}^{-1}, \boldsymbol{K}_2 = \boldsymbol{M}_0^{\mathrm{ref}}$$
$$\mathrm{DM}: \boldsymbol{K}_1 = 1/V_{\mathrm{dc}}^{\mathrm{ref}}, \boldsymbol{K}_2 = 0 \quad (6)$$

the admittance under the CM or the DM case can be determined. The detailed steps required for the harmonic-domain modeling of the studied system are presented in Appendix A.

2) Grid Harmonic-Domain Impedance: The grid harmonic-domain impedance of this article is straightforward, which is

$$\boldsymbol{Z}_g^{\mathrm{HTF}}(s) = \mathrm{diag}\left(\cdots, Z_{g(-1)}(s), Z_{g(0)}(s), Z_{g(+1)}(s), \cdots\right) \quad (7)$$

TABLE I
MAIN CIRCUIT AND CONTROL PARAMETERS

Circuit parameters		Control parameters
U_{N} = 200 V(rms)	L_{g} = 6.6 mH	H_{PLL}: k_{ppll} = 0.1, k_{ipll} = 100
I_{N} = 7 A (rms)	R_{g} = 0.258 ohm	H_{PR}: k_{pc} = 20, k_{ic} = 628
L_{f} = 3.3 mH	C_{cap} = 200 uF	H_{dc}: k_{pdc} = 5*10^{-5}, k_{idc} = 2.5*10^{-4}
R_{f} = 0.129 ohm	V_{dcN} = 320 V	k_{QSG} = 5.0
f_{sw} = 10 kHz	f_{sample} = 50 kHz	T_{d} = 50 us

where $\boldsymbol{Z}_g^{\mathrm{HTF}}(s)$contains the frequency-shifted copies of $Z_{g(0)}(s)$ and $Z_{g(0)}(s) = R_g + sL_g$.

D. HTF Truncation and VSC-MIMO Admittance Analysis

Practically, the truncated version of $\boldsymbol{Y}_c^{\mathrm{HTF}}(s)$ and $\boldsymbol{Z}_g^{\mathrm{HTF}}(s)$ is adopted for numerical analysis. If the HTFs are truncated to a harmonic order of N, then they can be generally represented by a $(2N+1)$-by-$(2N+1)$ dimensional matrix, as shown in (8) at the bottom of the next page. In later analysis, the truncated VSC-HTF and grid-HTF model are denoted by the *VSC-MIMO admittance* [e.g., $\boldsymbol{Y}_c^{N\times N}(s)$] and the *grid-MIMO impedance* [e.g., $\boldsymbol{Z}_g^{N\times N}(s)$].

The choice of harmonic order N for truncation is important for model accuracy. Prior knowledge regarding the number of dominant frequency couplings in the system is helpful. In this regard, it is already noticed that the MFC effect (i.e., $\pm f_p$ and $\mp f_p + 2f_1$) due to *dq* asymmetry of VSC controls (e.g., PLL) is a dominant component for balanced three-phase VSCs. Qualitatively, the frequency response of the single-phase VSC will at least contain components $\pm f_p$ and $\pm f_p \pm 2f_1$ due to the ac/dc modulation process. Thus, at least $N = \pm 2$ should be selected for HTF truncation. Different from the MFC in three-phase VSC, frequency responses at $\pm f_p \pm 2f_1$ are not only related to *dq* asymmetry of VSC controls but also affected by the second harmonic in the dc voltage. In addition, the triple harmonic on the ac side could also be relevant for modeling. Therefore, in this article, $N = \pm 3$ is selected for truncation, and the resulting VSC-MIMO admittance is denoted by $\boldsymbol{Y}_c^{7\times 7}(s)$.

To better visualize the frequency coupling effect, the VSC-MIMO admittance $\boldsymbol{Y}_c^{7\times 7}(s)$ under both the CM and DM cases will be plotted together with the measured frequency response from PSCAD/EMTDC (main parameters are listed in Table I). Due to the limited space, only the magnitude response is shown, and the *Y*-axis of subfigures is scaled to an identical range $[10^{-3}, 10^{-1}]$ to highlight the dominant components.

As shown in Fig. 2(a), magnitude responses under either of the cases are primarily located at the diagonals $Y_{c(k)}^{7\times 7}, k = 0, \pm 2, \pm 4$ [the subscript k denotes the element in (8)] since other responses present null values in the defined scale. Also, for each two of adjacent diagonals, they are separated by $2\omega_1$, which means the frequency coupling existent in this system is primarily related to components at $\pm f_k$ and $\pm f_k \pm 2f_1$, where $f_k = f_p + kf_1$ are

$$\boldsymbol{Y}_c^{\mathrm{HTF}}(s) = -\boldsymbol{C}_i \begin{bmatrix} s\boldsymbol{I} + \boldsymbol{N}_{\mathrm{blk}} - \boldsymbol{A}_c - \\ \boldsymbol{B}_m \boldsymbol{G}_{\mathrm{del}} \boldsymbol{K}_1 \left[2\boldsymbol{H}_{\mathrm{PR}} \boldsymbol{A}_{\cos}(\delta_{\mathrm{pll0}}) \boldsymbol{H}_{\mathrm{dc}} \boldsymbol{U}_{\mathrm{dc0}} - \boldsymbol{K}_2 - \boldsymbol{H}_{\mathrm{PR}}\right] \begin{bmatrix} \boldsymbol{C}_{\mathrm{dc}} \\ \boldsymbol{C}_i \end{bmatrix} \end{bmatrix}^{-1} \left(\boldsymbol{B}_u - \boldsymbol{B}_m \boldsymbol{G}_{\mathrm{del}} \boldsymbol{U}_{\mathrm{dc0}}^{-1} \boldsymbol{H}_{\mathrm{PR}} \boldsymbol{I}_{b0}^{\mathrm{ref}} \boldsymbol{G}_{\theta\_u}\right) \quad (5)$$

the shifted copies of f_p. This observation justifies the aforementioned dominant frequency components in the system. Besides, responses away from the central diagonal are gradually reduced, e.g., components in $Y^{7\times7}_{c(\pm4)}$ are much smaller than those in $Y^{7\times7}_{c(\pm0)}$. On the other hand, magnitude responses under the CM case are different from those under the DM case (see Fig. 2(b)) in particular, the differences are evident for components away from the central diagonal. This analysis implies that a smaller steady-state harmonic can bring a lower extent of frequency couplings.

Overall, this VSC-MIMO admittance analysis indicates that 1) the order of this VSC-MIMO admittance $(N = \pm3)$ can be further reduced since the magnitude responses away from the central diagonal are decaying in a great extent, and 2) characteristics of the VSC-MIMO admittance under the CM and DM cases are not the same, which implies that impacts on model simplification are expected. These two main findings will be discussed more in detail after the introduction of the SISO equivalent modeling techniques.

III. SISO Equivalent Modeling Technique and Comparative Analysis of VSC Reduced-Order Models

The developed VSC-MIMO admittance $\boldsymbol{Y}_c^{7\times7}(s)$is rather complicated to analyze and implement due to the large model dimension. For instance, to measure this 7-by-7 matrix, seven independent perturbations should be used at each frequency point, which is cumbersome for frequency sweeping. In regard to stability analysis, although the generalized Nyquist criterion can be used [32], stability assessment is not intuitive due to the presence of multiple eigenloci. All these arguments point to the benefits of using a SISO model.

The most simplified SISO model is the component $Y^{7\times7}_{c(0)}(s)$ in $\boldsymbol{Y}_c^{7\times7}(s)$. Clearly, this SISO model ignores all the frequency coupling effects and may not be useful for analysis. In order to preserve the frequency couplings while using the SISO representation, Zhang *et al.* [33] introduced an equivalent SISO modeling by viewing the grid and VSC as a closed-loop system. Starting from the approach in [33], this section will present the SISO equivalent modeling technique applied to the harmonic domain.

A. Principle of the MIMO to SISO Conversion

In essence, the previously derived VSC and grid MIMO models (i.e., $\boldsymbol{Y}_c^{N\times N}(s)$ and $\boldsymbol{Z}_g^{N\times N}(s)$) are defined in an open-loop sense. When they are connected, they will form a closed system, and interactions will occur among them. As illustrated in Fig. 3(a), if the VSC is perturbed at ω_p by an independent voltage source, the current responses will not only contain the component at ω_p but also contain harmonics at $\omega_p + k\omega_1,\ k = \pm1 \ldots \pm N$ according to $\boldsymbol{Y}_c^{N\times N}(s)$. When flowing through the grid impedance $\boldsymbol{Z}_g^{N\times N}(s)$, the current responses of the VSC will induce harmonic voltages at the grid side as $\boldsymbol{U}_{g(k)}(\omega_p), k = 0, \pm1, .., \pm N$. Also, since there is only one independent source $\boldsymbol{U}_{ptb}(\omega_p)$ in the circuit, the harmonic voltages of the VSC and grid must comply with $\boldsymbol{U}_{g(\pm k)}(\omega_p) = \boldsymbol{U}_{a(\pm k)}(\omega_p),\ k \neq 0$, which means they are mutually dependent.

From the abovementioned illustration and Fig. 3, it can be found that viewing the grid VSC as a closed-loop system, the dependent paths can be eliminated from circuit operations. Thus, an equivalent relation of the input voltage and output current under the same frequency ω_p can be established, which corresponds to the SISO equivalent model of this article.

B. Method for Deriving the SISO Equivalent Model

To make the circuit operations easier, the columns and rows of the $\boldsymbol{Y}_c^{N\times N}(s)$ and $\boldsymbol{Z}_g^{N\times N}(s)$ are rearranged so that they can be compactly represented by vectors or submatrix blocks. The concept to achieve this rearrangement is shown in Fig. 3(b), where it is indicated how the columns and rows of $\boldsymbol{Y}_c^{7\times7}(s)$ are sequentially switched until the component $Y^{7\times7}_{c(0)}(s)$ is moved to the left-top corner of the matrix.

Thus, for an *N*-order model of the VSC and grid, the following equations can be established:

$$-\begin{bmatrix} I_{a(0)}(s) \\ \boldsymbol{I}_{ah}(s) \end{bmatrix} = \begin{bmatrix} Y^{N\times N}_{c(0)} & \boldsymbol{a}_{1\times2N} \\ \boldsymbol{b}_{2N\times1} & \boldsymbol{Q}_{2N\times2N} \end{bmatrix} \begin{bmatrix} U_{a(0)}(s) \\ \boldsymbol{U}_{ah}(s) \end{bmatrix}$$

$$\begin{bmatrix} U_{g(0)}(s) \\ \boldsymbol{U}_{ah}(s) \end{bmatrix} = \begin{bmatrix} Z^{N\times N}_{g(0)} & \boldsymbol{0}_{1\times(2N-1)} \\ \boldsymbol{0}_{(2N-1)\times1} & \boldsymbol{c}_{2N\times2N} \end{bmatrix} \begin{bmatrix} I_{a(0)}(s) \\ \boldsymbol{I}_{ah}(s) \end{bmatrix} \quad (9)$$

where $Y^{N\times N}_{c(0)}, \boldsymbol{a}_{1\times2N}, \boldsymbol{b}_{2N\times1},$ and $\boldsymbol{Q}_{2N\times2N}$ are known components that can be extracted from $\boldsymbol{Y}_c^{N\times N}(s)$. $\mathbf{c}_{2N\times2N} = \mathbf{Z}^{N\times N}_{g(\mathrm{k})}, k \neq 0, \boldsymbol{I}_{ah}(s) = [I_{a(-N)}, \ldots, I_{a(k)}, \ldots, I_{a(+N)}]^T$, and $\boldsymbol{U}_{ah}(s)$ $(k \neq 0)$ has a format similar to $\boldsymbol{I}_{ah}(s)$.

According to Fig. 3(a) and (9), there are $2(2N+1)+2$ unknown variables (i.e., $\boldsymbol{U}_{a(\pm k)}, \boldsymbol{I}_{a(\pm k)}, \boldsymbol{U}_{ptb}, \boldsymbol{U}_{g(0)}$) and $2(2N+1)+1$ sets of known equations. The remaining augmented equation that is not shown in (9) can be derived from Fig. 3(a) as $\boldsymbol{U}_{ptb} + \boldsymbol{U}_{g(0)} = \boldsymbol{U}_{a(0)}$. Based on this, the relation of $\boldsymbol{U}_{a(0)}$ and $\boldsymbol{I}_{a(0)}$ can be established, which is written as

$$-I_{a(0)}(s) = \underbrace{\left(Y^{N\times N}_{c(0)} - \boldsymbol{a}_{1\times2N}(\boldsymbol{I} + \boldsymbol{c}_{2N\times2N}\boldsymbol{Q}_{2N\times2N})^{-1}\boldsymbol{c}_{2N\times2N}\boldsymbol{b}_{2N\times1}\right)}_{Y_c^{\mathrm{SISO}}(s)} \cdot U_{a(0)}(s) \quad (10)$$

$$\boldsymbol{H}^{N\times N}(s) = \begin{bmatrix} H_{(0)}(s - jN\omega_1) & \cdots & H_{(-N)}(s) & \cdots & H_{(-2N)}(s + jN\omega_1) \\ \vdots & \ddots & \vdots & \ddots & \vdots \\ H_{N}(s - jN\omega_1) & \ddots & H_{(0)}(s) & \ddots & H_{(N)}(s + jN\omega_1) \\ \vdots & \ddots & \vdots & \ddots & \vdots \\ H_{(2N)}(s - jN\omega_1) & \cdots & H_{(+N)}(s) & \cdots & H_{(0)}(s + jN\omega) \end{bmatrix} \quad (8)$$

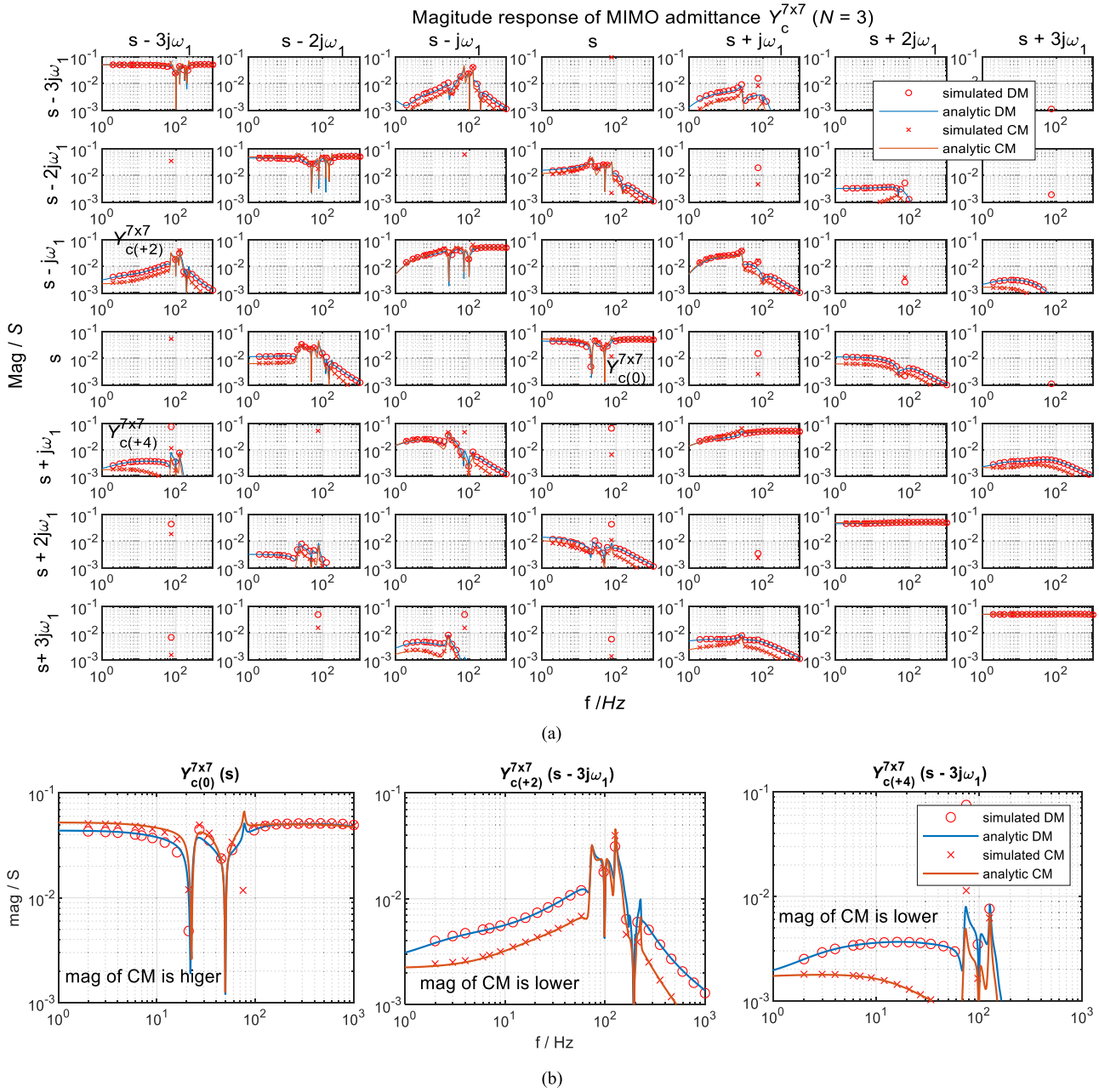

Fig. 2. Magnitude responses of the VSC-MIMO admittance ($N = \pm 3$ and $I_q^{\text{ref}} = -3\text{A},\ R_L = 1e5\ \Omega$). (a) VSC-MIMO admittance plot. (b) Zoomed-in plots of the extracted three components.

and the grid-SISO model is

$$U_{g(0)}(s) = Z_{g(0)}^{N\times N}(s)\, I_{a(0)}(s) = Z_g^{\text{SISO}}(s)\, I_{a(0)}(s). \quad (11)$$

It can be seen that the derived VSC-SISO admittance $Y_c^{\text{SISO}}(s)$ is composed of two terms, the first term $Y_{c(0)}^{N\times N}$ reflects the relation of input and output at the same frequency, whereas the second term reflects the effects of the harmonic interactions between the grid and the VSC. Furthermore, when the Nyquist-based stability analysis is performed, it has been proven in [33] that the SISO equivalent system has an identical critical stability condition to that of the original MIMO system, a similar proof based on a simplified representation of the cases studied is presented in Appendix B. Therefore, the presented SISO equivalent modeling technique itself will not compromise the accuracy in analysis.

C. Comparative Analysis of the VSC Full- and Reduced-Order Admittances by Using the SISO Modeling Technique

Based on the abovementioned method, VSC reduced-order models from different truncations of $\boldsymbol{Y}_c^{7\times7}(s)$ can be effectively compared via their SISO equivalents. In Fig. 4, the following VSC models of different orders are considered for comparison.

1) The *full-order model* uses all the components of $\boldsymbol{Y}_c^{7\times7}(s)$.

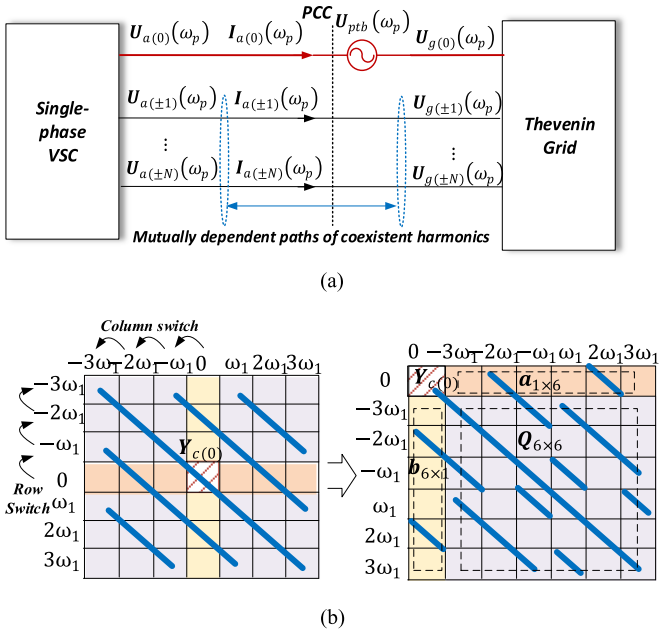

Fig. 3. Principle and method of MIMO to SISO conversion. (a) Circuit illustration of the harmonic interactions. (b) Illustration of the matrix rearrangement.

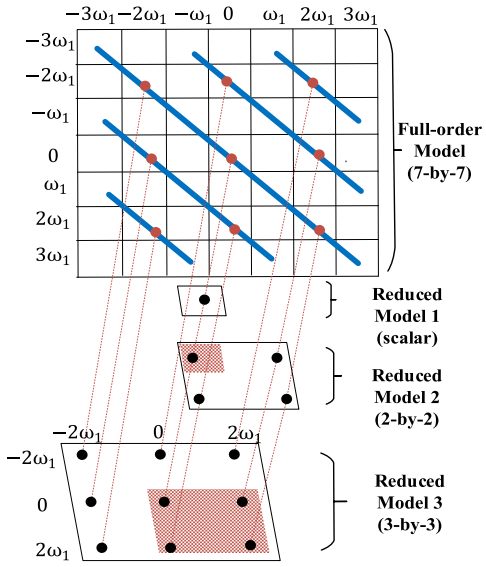

Fig. 4. Extraction of the reduced VSC-MIMO admittances.

2) The reduced-order *Model 1* directly uses the component $Y_{c(0)}^{7\times7}(s)$ of $\boldsymbol{Y}_c^{7\times7}(s)$, and thus this is a scalar model.
3) The reduced-order *Model 2* extracts the frequency components f_p and $f_p + 2f_1$ from $\boldsymbol{Y}_c^{7\times7}(s)$, and thus, it is a 2×2 matrix model and resembles the ones presented in [26]–[29].
4) The reduced-order *Model 3* extracts the frequency components f_p and $f_p \pm 2f_1$ from $\boldsymbol{Y}_c^{7\times7}(s)$, and thus it is a 3-by-3 matrix model and resembles the one presented in [30]. Notations of corresponding SISO equivalent models are listed in Table II.

In order to test these models under a relatively critical condition, i.e., with low stability margin, the current controller gain

TABLE II
NOTATIONS OF DIFFERENT SISO EQUIVALENTS

Name	MIMO model dimension	SISO model notation
Full-order model	7x7	$Y_{\text{c\_full}}^{\text{SISO}}$
Reduced-order model 1	scalar	$Y_{\text{c\_rm1}}^{\text{SISO}}$
Reduced-order model 2	2x2	$Y_{\text{c\_rm2}}^{\text{SISO}}$
Reduced-order model 3	3x3	$Y_{\text{c\_rm3}}^{\text{SISO}}$

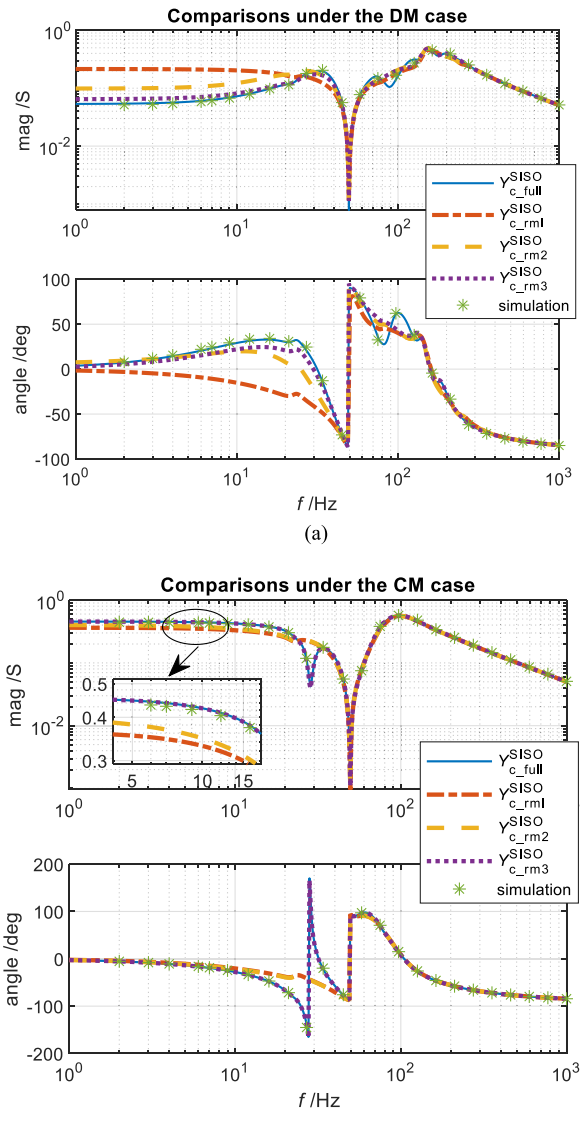

Fig. 5. SISO-equivalent-based comparative analysis of reduced-order VSC admittances ($k_{\text{pc}} = 2$, dc voltage control gain is doubled, $I_q^{\text{ref}} = -3$ A, $R_L = 1e5\ \Omega$, other configurations are identical to Table I). (a) Comparisons under the DM case. (b) Comparisons under the CM case.

is reduced, whereas the dc voltage controller gain is increased. Similar conditions with low stability margin state can occur in practical situations, e.g., for operation in weak ac grids.

According to the comparative results presented in Fig. 5, the SISO model $Y_{\text{c\_full}}^{\text{SISO}}$ converted from the full-order MIMO model is consistent with measurements and is accurate under both the

TABLE III
SUMMARY OF THE MODEL REDUCTION ANALYSIS

Name	SISO model notation	Accuracy DM case	Accuracy CM case
Full-order model	$Y_{\text{c\_full}}^{\text{SISO}}$	Accurate	Accurate
Reduced-order model 1	$Y_{\text{c\_rm1}}^{\text{SISO}}$	Low	Medium
Reduced-order model 2	$Y_{\text{c\_rm2}}^{\text{SISO}}$	Medium (−)	Medium (+)
Reduced-order model 3	$Y_{\text{c\_rm3}}^{\text{SISO}}$	High	Accurate

CM and DM cases. Thus, $Y_{c\_\text{full}}^{\text{SISO}}$ will be used as the reference model for later comparisons.

The model accuracy of different truncations under the DM case is compared and shown in Fig. 5(a). The accuracies of the reduced-order VSC models, if ranked in a descending sequence, is given by $Y_{c\_rm3}^{\text{SISO}} > Y_{c\_rm2}^{\text{SISO}} > Y_{c\_rm1}^{\text{SISO}}$. From the plots, it can be seen that $Y_{c\_rm3}^{\text{SISO}}$ only has small differences from $Y_{c\_\text{full}}^{\text{SISO}}$ under the DM case. Thus, its accuracy is defined as *High*. Besides, $Y_{c\_rm2}^{\text{SISO}}$ exhibits evident discrepancies from $Y_{c\_\text{full}}^{\text{SISO}}$, and thus its accuracy is defined as *Medium* $(-)$, whereas the accuracy of $Y_{c\_rm1}^{\text{SISO}}$ is defined as *Low* if compared with the accuracy of $Y_{c\_rm2}^{\text{SISO}}$.

Next, model accuracies under the CM case are compared and shown in Fig. 5(b). Overall, the model accuracies of reduced-order VSC models are improved compared with the DM case. In detail, $Y_{c\_rm3}^{\text{SISO}}$ is as accurate as $Y_{c\_\text{full}}^{\text{SISO}}$ under this CM case. Furthermore, $Y_{c\_rm1}^{\text{SISO}}$ and $Y_{c\_rm2}^{\text{SISO}}$ are almost close to $Y_{c\_\text{full}}^{\text{SISO}}$ in terms of admittance shapes although one of the resonances is wrongly predicted. Also, it is noted that the differences between $Y_{c\_rm2}^{\text{SISO}}$ and $Y_{c\_rm1}^{\text{SISO}}$ are very small though $Y_{c\_rm2}^{\text{SISO}}$ turns out to be slightly more accurate (as can be seen from the zoom-in subfigure). Thus, their accuracies are defined as Medium $(-)$ and Medium $(+)$, respectively. A summary of this analysis is shown in Table III.

IV. COMPARATIVE STABILITY ANALYSIS OF THE CM AND DM CASES BY USING THE SISO IMPEDANCES

The previous analysis has shown that reduced-order models exhibit different accuracies under the CM and DM cases. This implies that stability differences may also exist, which is interesting to investigate. In this section, the effect of the CM in comparison with the DM case will be analyzed by using the full-order SISO impedance $Y_{c\_\text{full}}^{\text{SISO}}$.

A. Qualitative Analysis of the CM Effect

According to the harmonic-domain modeling presented in Appendix A, the overall system is represented in Fig. 6. It can be seen that the main model difference between the CM and the DM lies in the parameters $\boldsymbol{K}_1$ and $\boldsymbol{K}_2$, where $\boldsymbol{K}_1 = \boldsymbol{U}_{\text{dc0}}^{-1}$ and $\boldsymbol{K}_2 = \boldsymbol{M}_{a0}^{\text{ref}}$ for the CM case and $\boldsymbol{K}_1 = 1/V_{\text{dc}}^{\text{ref}}$ and $\boldsymbol{K}_2 = 0$ for the DC case according to (6).

Furthermore, if $\boldsymbol{M}_{a0}^{\text{ref}} = 0$ holds true, then the CM model and DM model will be approximately the same. However, this condition is barely valid since the VSC needs to output an ac voltage that is comparable to the grid, i.e., $\boldsymbol{M}_{a0}^{\text{ref}} \neq 0$. This means that the model difference always exists, and this difference is reflected in the additional feedback loop gain $\boldsymbol{M}_{a0}^{\text{ref}}$ of the CM case. This gain effect can also be physically interpreted as a sort of damping to the VSC circuit, whereas the sign of this damping yet remains to be determined.

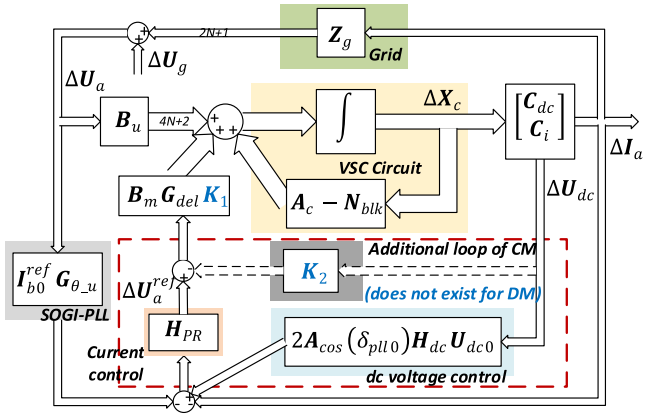

Fig. 6. Harmonic-domain control diagram of the single-phase grid-VSC system.

To evaluate the additional damping characteristic present in the CM model (i.e., positive or negative), a straightforward way is to change $\boldsymbol{M}_{a0}^{\text{ref}}$ and see how it shapes the admittance. However, $\boldsymbol{M}_{a0}^{\text{ref}}$ cannot be operated directly since it is not an independent control variable. To overcome this issue, the gain of the parallel control loop can be changed instead, and the resulting effect will be approximately the same as changing the gain of $\boldsymbol{M}_{a0}^{\text{ref}}$. For instance, the effect of increasing the gain $\boldsymbol{M}_{a0}^{\text{ref}}$ can be qualitatively studied by reducing the parallel control loop gain, where the latter one can be readily fulfilled by reducing the current controller gain.

B. Negative Damping Characteristic of the CM Effect

Based on the abovementioned method, $Y_{c\_\text{full}}^{\text{SISO}}$ under two types of current controller gains are compared to identify the damping characteristic. As can be seen from Fig. 7, overall, the VSC-SISO admittance under the CM case has higher magnitudes than those of the DM case. From the impedance-based analysis perspective, it can be obtained that a larger VSC admittance will result in a larger impedance ratio so that the stability margin is lowered. This implies that the CM case is less stable than the DM case, and thus this additional damping effect presented in the CM case is expected to be negative.

To further study the incremental effect of $\boldsymbol{M}_{a0}^{\text{ref}}$ to the CM model itself, the VSC-SISO admittances of the CM case under $k_{\text{pc}} = 8$ and $k_{\text{pc}} = 4$ are compared. It can be seen that the magnitude response is increased as the current controller gain is reduced, and thus a lower stability margin is anticipated. This observation in combination with the previous interpretation that the effect of reducing the current controller gain is equivalent to the effect of increasing $\boldsymbol{M}_{a0}^{\text{ref}}$ indicates that this incremental effect of $\boldsymbol{M}_{a0}^{\text{ref}}$ to the CM model itself is negative. Based on the abovementioned two aspects, it can be concluded that this CM gain effect has a negative damping characteristic.

Furthermore, in order to directly study the stability effect, in the following section, the Nyquist-based analysis will be performed.

C. Comparative Stability Analysis of the CM and DM Cases

A classic source and load system partitioned at the point of common coupling (PCC) and based on the SISO equivalent

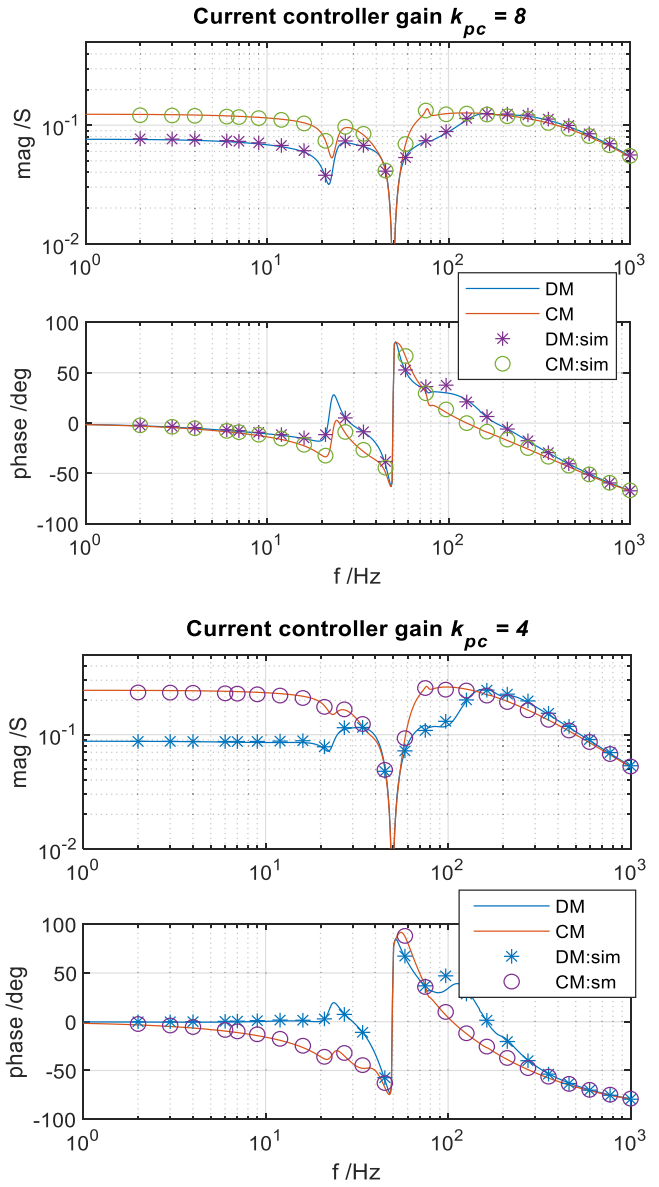

Fig. 7. VSC-SIO admittance comparisons of the CM and DM cases ($I_q^{\text{ref}} = -3$ A, $R_L = 1e5\ \Omega$, and other configurations presented in Table I remain unchanged).

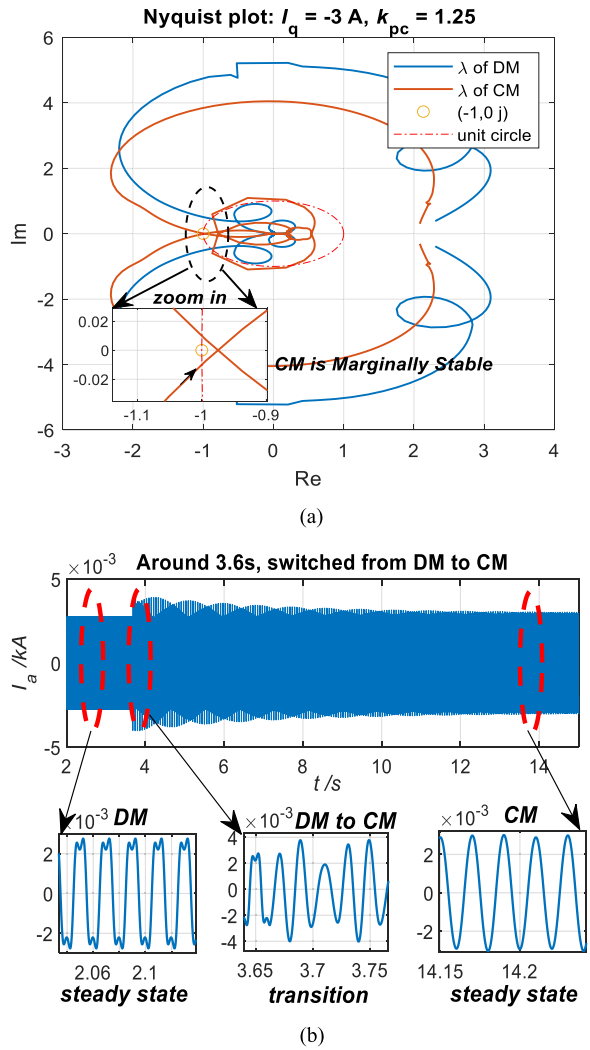

Fig. 8. Comparative stability analysis and time-domain verification of the CM and DM ($k_{\text{pc}} = 1.25$, other parameters are identical to Table I). (a) Nyquist plots comparison of the CM and DM cases. (b) Time-domain ac current waveforms.

models can be established according to the work presented by Sun [6]. Thus, the impedance ratio of the closed-loop system can be formulated, from which the Nyquist diagram can be drawn. For this study, the impedance ratio is derived as $L(s) = Y_{\text{c\_full}}^{\text{SISO}} Z_{g(0)}^{\text{SISO}}$.

In Fig. 8(a), Nyquist plots of the DM and CM cases are compared under a smaller current controller gain (i.e., $k_{\text{pc}} = 1.25$), while other configurations are identical to the ones presented in Table I. Under such a condition, both the CM and DM cases conclude a stable system (there are no right-half-plane poles in this case). However, it is noticed that the stability margin of the CM case is much lower than that of the DM case, verifying the negative damping effect. In fact, the DM case of this study is a marginally stable system since one of its eigenloci is close to the critical point $(-1, 0\,j)$ when it crosses the real axis.

To verify the conclusion from the Nyquist-based stability analysis, time-domain simulation in PSCAD/EMTDC is conducted, where the VSC initially operates in the DM case, and then it is switched to the CM case at 3.6 s. The current response from this simulation is shown in Fig. 8(b), from which it can be confirmed that the system is marginally stable under the CM case since the current response is weakly damped.

Besides, from the magnified plots, it can be observed that the steady-state current waveform of the CM case is much better than the DM case. This is a known benefit of CM but, as identified in this analysis, the CM will push the system more toward the stability margin. It is worth mentioning that this analysis is conducted in a low-margin state on purpose, where the waveform of the DM case seems not acceptable. However, if the overall system margin is improved, the DM case can also provide decent power quality. Besides, additional features could be included in the control system to improve the stability margin of the CM case.

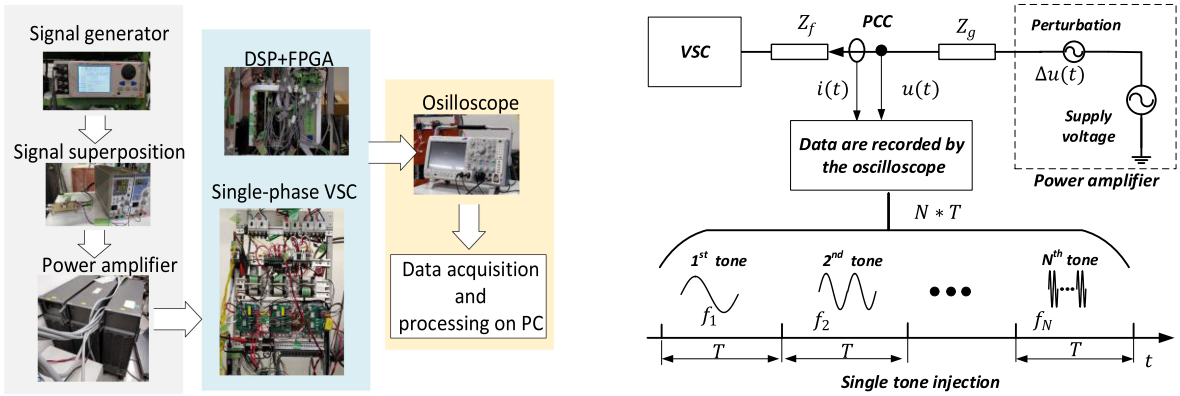

Fig. 9. Experimental setup for SISO impedance measurement verification. (a) Experimental system layout. (b) Illustration of impedance measurement.

V. Experimental Verification

This section presents experimental impedance measurement and verification of the developed full-order VSC-SISO admittance, i.e., $Y_{c\_\text{full}}^{\text{SISO}}$ along with some experimental stability tests to consolidate the theoretical analyses.

A. Experimental Setup

The experimental setup is briefly illustrated in Fig. 9(a), which is composed of a signal generator, an analog superposition circuit, a linear amplifier, a single-phase VSC, and an oscilloscope. The VSC control system is implemented in a digital controller based on the PE-expert4 platform, with a control cycle $T_d = 50\ \mu$s.

Regarding the SISO admittance measurement, both the supply voltage and the small-signal perturbation voltage are generated by the signal generator, however, from separate output channels. Thus, an analog circuit shown in Fig. 9(a) is used to superimpose the signals and send them to the power amplifier [see the depiction in Fig. 9(b)]. The single-tone injection method is applied, which means for a specific time interval *T*, only one specified frequency is injected into the system. Then, this method is repeated for each frequency ranging from 5 Hz to 1 kHz. The time interval *T* used in this experiment is 6 s to assure the system reaches a good steady state in this period and to avoid the influence of transients when injecting a new perturbation. Voltage and current data are recorded by the oscilloscope and exported to MATLAB for impedance calculation and analysis (the sampling rate is 50 kHz, and the window for discrete Fourier analysis is 5 s).

B. Experimental Verification of the VSC-SISO Admittance

The admittance verification was conducted under both the CM and DM cases. Main circuit and control parameters are listed in Table I, and the following two cases are considered.

Case I: $I_q^{\text{ref}} = -3$ A, $R_L = 1e5\ \Omega$, i.e., a reactive power load condition.

Case II: $I_q^{\text{ref}} = 0$A, $R_L = 128\ \Omega$ (i.e. $I_d^{\text{ref}} \approx -6$ A), i.e., an active power load condition.

The comparative results are shown in Fig. 10, from which it can be seen that the full-order VSC-SISO admittance $Y_{c\_\text{full}}^{\text{SISO}}$ is basically consistent with the experimental results for all the scenarios (i.e., under the CM and the DM case, and under different operating points). At the highest frequencies, small deviations between the model and the experiments can be noticed, mainly due to the influence of the sampling effects and frequency and temperate dependencies of parameters that are not represented in the analytical model. However, a point-to-point match is achieved when compared with the simulated results where the abovementioned issues are greatly alleviated. This analysis proves that the developed full-order VSC-SISO admittance $Y_{c\_\text{full}}^{\text{SISO}}$ is effective and accurate, and this also indicates that the MIMO to SISO conversion technique is valid.

Besides, from the comparisons, it can also be noticed that the operating conditions have evident impacts on the admittance characteristics as well.

TABLE IV
Theoretical Parameters for Stability Tests

Parameters	DM case	CM case
H_{PR}	$k_{\text{pc}} = 2$, $k_{\text{ic}} = 2$	$k_{\text{pc}} = 1$, $k_{\text{ic}} = 2$
H_{dc}	$k_{p\text{dc}} = 5*10^{-5}$ $k_{\text{idc}} = 0.05$	$k_{\text{pdc}} = 5*10^{-5}$ $k_{\text{idc}} = 2.5*10^{-4}$
H_{pll}	k_{ppll} =0.1, k_{ipll} =100	
Load	$I_{\text{q}}^{\text{ref}} = -3\ A, R_{\text{load}} = 10^5\ ohm$	
Others	The same as Table I	

C. Experimental Stability Tests

This section presents experimental stability tests under both the DM and the CM cases along with further justifications on model accuracy and damping analysis, in which, the marginally unstable condition is focused. Such a condition is achieved by continuously varying the control parameters until the marginally unstable state appears in the Nyquist plot. Corresponding control parameters for the CM and the DM cases are registered and listed in Table IV. Then, these theoretically predicted control parameters will be applied in the experimental system to observe whether the marginally unstable state will occur or not. It should be noted that before this change, control parameters presented in Table I are adopted to assure a stable state.

An experimental stability test under the DM case is first conducted and analyzed. According to the Nyquist plot shown in Fig. 11(a), the system will be marginally unstable due to the clockwise encirclement of the critical point (no right-half-plane

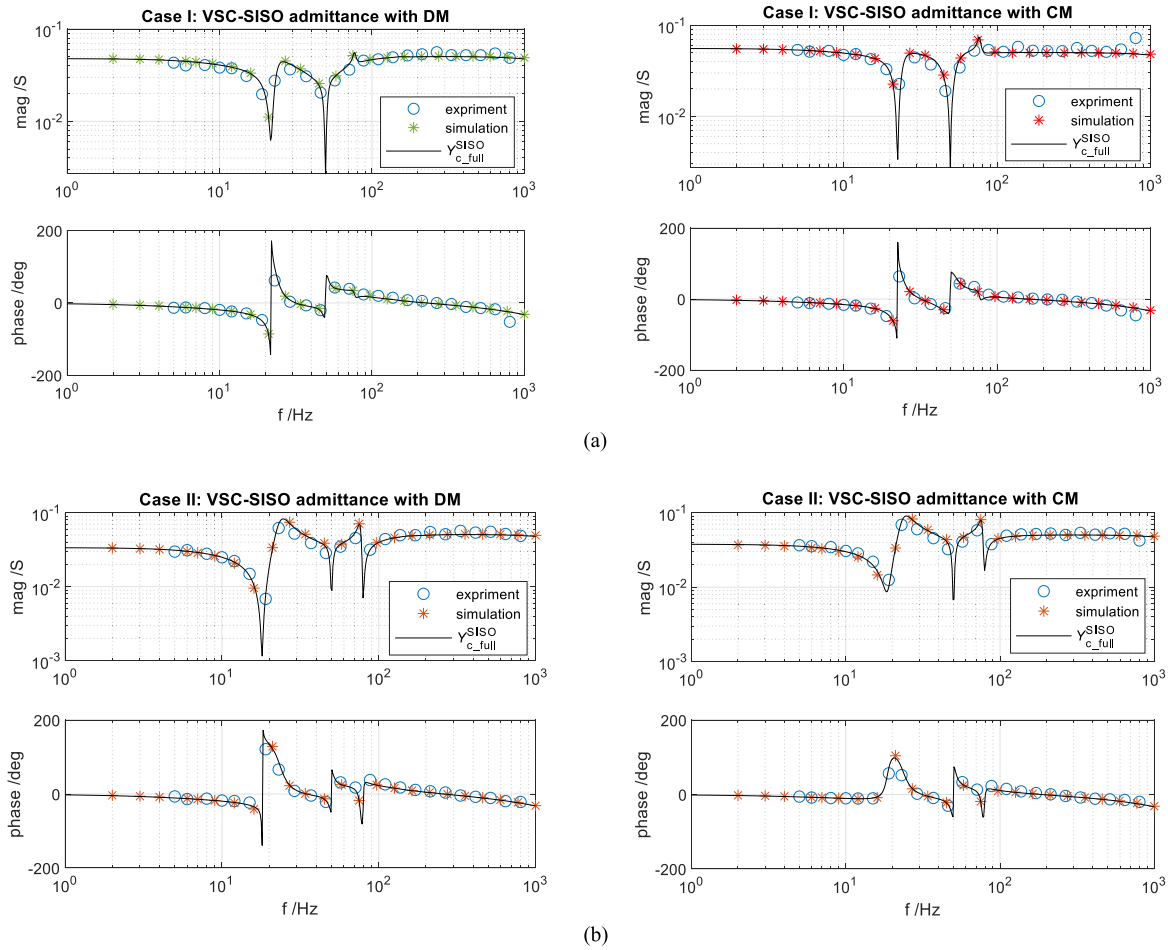

Fig. 10. Experimental verification of the full-order VSC-SISO admittance model (Case I, $I_q^{\text{ref}} = -3\text{A}$, $R_L = 1e5\ \Omega$; Case II, $I_q^{\text{ref}} = 0\text{A}$, $R_L = 128\ \Omega$ (i.e. $I_d^{\text{ref}} \approx -6\text{ A}$)). (a) VSC-SISO admittance comparisons under Case I. (b) VSC-SISO admittance comparisons under Case II.

open-loop poles). The corresponding control parameters are listed in Table IV. After setting these new control parameters to the experimental system around 9.5 s, the system gradually becomes oscillatory as can be seen from the time-domain waveforms, proving that the Nyquist-based analysis is correct. Also, from the dc voltage and ac current spectra, it can be obtained that the dc-side oscillation frequency of this case study is around 50 Hz, and this oscillation leads to two evidently coupled frequency components on the ac side, which are at the dc and the 100 Hz. Moreover, the magnitudes of the ac current at these two frequency components are different, implying an asymmetric oscillation similar to the MFC effect of a three-phase VSC.

Next, a similar stability test under the CM case is conducted, and the results are shown in Fig. 11(b). From the Nyquist plot, it is obtained that the system will be marginally unstable due to the encirclement. This conclusion is justified by the experimental waveforms in which instability occurs after the new parameters are set in the experimental system. The dc-side oscillation frequency of this case is around 15 Hz, as a result, the ac side presents two evidently coupled frequency components at 35 Hz and 75 Hz.

The two presented stability tests further consolidate the validity of the proposed model and the Nyquist-based analysis. Besides, it is noticed that a simulated stability test under the CM case has been conducted in Fig. 8, where it concludes a marginally stable system with a current controller gain at $k_{\text{pc}} = 1.25$. However, as shown in this experimental stability test, in Fig. 11(b), if the current controller gain is reduced to $k_{\text{pc}} = 1$ while keeping other conditions unchanged from Fig. 8, the system stability condition is changed from marginally stable to marginally unstable. This conclusion confirms again that the additional damping characteristic of the CM case is negative.

VI. Conclusion

This article presents a SISO equivalent impedance modeling technique that enables a simple impedance measurement and stability analysis for the single-phase grid-connected VSC. The developed VSC-SISO admittance preserves all the frequency couplings presented in the HTFs, and thus they are equivalent in terms of model accuracy. Also, it is noted that since the overall impedance modeling is still based on the principle of switch-averaging, the resulting model is mainly valid for control-related stability analysis, in which the frequency range is far below the switching frequency. For this purpose, the developed VSC-SISO admittance is experimentally verified below 1 kHz.

Applications of the SISO modeling technique for the VSC model reduction and stability characteristic analysis, under the

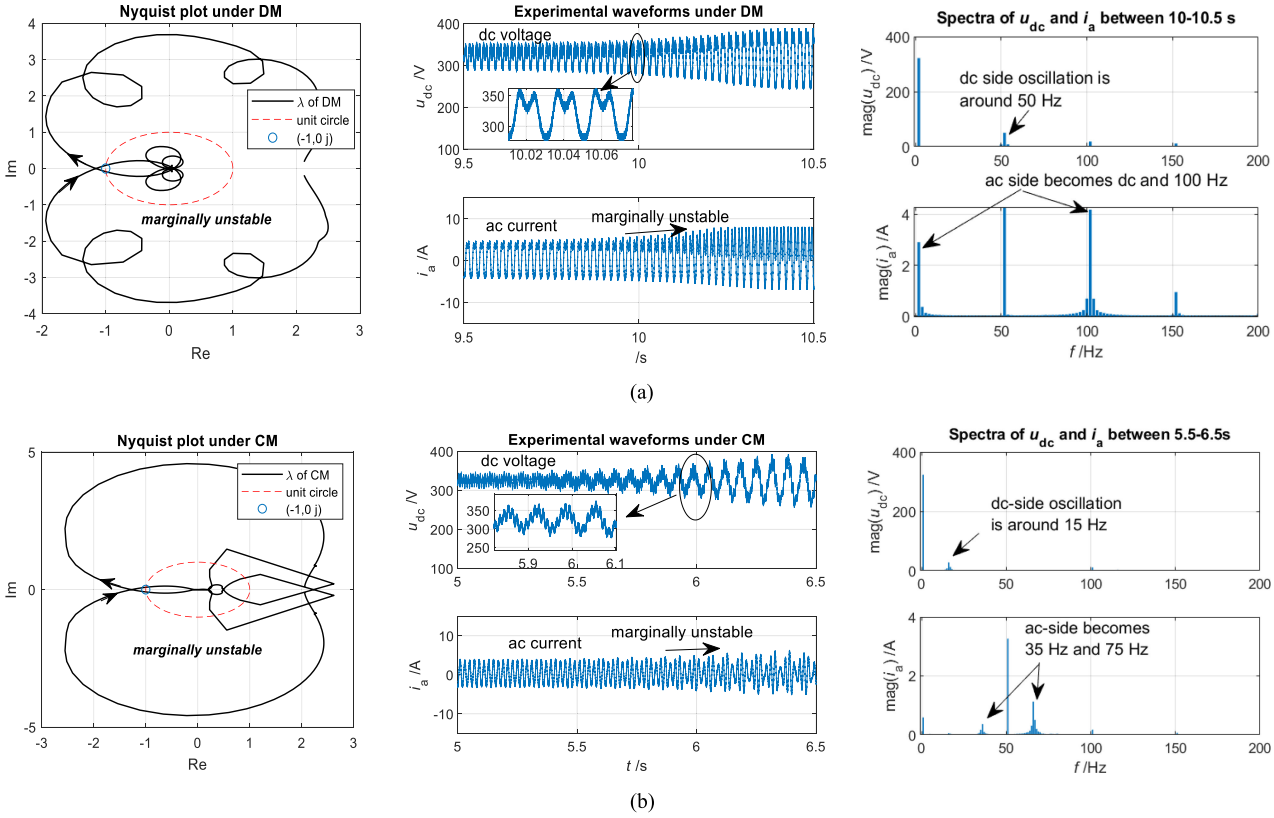

Fig. 11. Experimental stability tests under the CM and the DM cases. (a) Stability test under the DM case. (b) Stability test under the CM case.

CM and DM cases (i.e., with and without compensating the dc voltage variation in VSC control), are presented. Some main conclusions are listed as follows.

1) Three reduced-order VSC models extracted from its HTF model are compared with respect to model accuracy. The 3-by-3 matrix model characterizing the frequency components $f_p, f_p \pm 2f_1$ is accurate in most cases. The 2-by-2 matrix model characterizing the frequency components $f_p, f_p - 2f_1$ performs decently overall, in particular, with relatively small steady-state harmonics (e.g., under the CM case). The scalar model characterizing the frequency component f_p has the lowest accuracy compared with others.
2) In terms of stability, the CM case exhibits an additional negative damping effect on the system compared with the DM case, i.e., the CM case is less stable. Thus, attention should be paid to this unfavorable stability influence from the CM case, though it has some benefits in power quality. Ancillary stabilization controls for the CM case are expected to be developed in future works, which can be better fulfilled based on the SISO modeling technique.

Finally, although the mathematical development of this SISO equivalent model is rather cumbersome, the process provides insightful evidence on the understanding and the consequences of SISO impedance measurement of an interconnected system with frequency couplings.

When measuring the VSC impedance only using the current and voltage at the same frequency, the information of frequency couplings will not be lost as long as such a measurement is conducted under a grid-connected condition. This concept is significantly useful for impedance-measurement-based analysis, where tedious modeling is not necessary. However, the presented approach also results in one drawback that the obtained VSC-SISO equivalent model is in a closed-loop sense and should always be updated in accordance with the grid conditions.

APPENDIX

A. Harmonic-Domain VSC Admittance Modeling

In the following sections, the detailed harmonic-domain impedance modeling process of the single-phase grid-VSC system, as shown in Fig. 1, will be presented.

1) Modeling of the SOGI-QSG PLL: Based on the control blocks shown in Fig. 1(b), the HTF of SOGI-based QSG is given as

$$\begin{bmatrix} \hat{\boldsymbol{U}}_a(s) \\ \hat{\boldsymbol{U}}_b(s) \end{bmatrix} = \begin{bmatrix} \boldsymbol{H}_{\mathrm{QSG}a}(s) \\ \boldsymbol{H}_{\mathrm{QSG}b}(s) \end{bmatrix} \boldsymbol{U}_a(s) \tag{A.1}$$

where $\boldsymbol{H}_{\mathrm{QSG}a,b}$ are composed of the frequency-shifted copies of $H_{\mathrm{QSG_a,b}}\,\boldsymbol{U}_{a,b}(s) = [\ldots, U_{a,b(-1)}, U_{a,b(0)}, U_{a,b(+1)}, ..]^T$.

Then, the linearized q-axis input of PLL is

$$\Delta u_q = \begin{bmatrix} -\sin\theta_{\mathrm{pll0}}(t) & \cos\theta_{\mathrm{pll0}}(t) \end{bmatrix} \begin{bmatrix} \Delta\hat{u}_a \\ \Delta\hat{u}_b \end{bmatrix} - \hat{U}_{d0}(t) \cdot \Delta\theta_{\mathrm{pll}} \tag{A.2}$$

where $\theta_{\mathrm{pll0}}(t) = \omega_1 t + \delta_{\mathrm{pll0}}$, and $\hat{U}_{d0}(t)$ is the steady-state d-axis grid voltage estimated by the QSG. Since the SOGI-QSG is very selective, the ac components of $\hat{U}_{d0}(t)$ will be greatly attenuated, and thus $\hat{U}_{d0}(t) \approx U_{d0}$ is obtained, where U_{d0} is the

dc component. Thus, the HTF model of (A.2) is

$$\Delta \boldsymbol{U}_q(s) = \left[-\boldsymbol{A}_{\sin}(\delta_{\text{pll0}})\ \boldsymbol{A}_{\cos}(\delta_{\text{pll0}})\right]\begin{bmatrix}\Delta\hat{\boldsymbol{U}}_a(s)\\ \Delta\hat{\boldsymbol{U}}_b(s)\end{bmatrix} - \boldsymbol{U}_{d0}\cdot\Delta\boldsymbol{\theta}_{\text{pll}}(s) \tag{A.3}$$

where $\boldsymbol{A}_{\sin}(\delta_{\text{pll0}}) = P\{\sin\theta_{\text{pll0}}\}$, within which the nonzero components are $A_{\pm1} = \mp 0.5j\cdot e^{\pm j\delta_{\text{pll0}}}$; whereas the nonzero components of $\boldsymbol{A}_{\cos}(\delta_{pll0})$ are $A_{\pm1} = \pm 0.5e^{\pm j\delta_{\text{pll0}}}$; $\boldsymbol{U}_{d0} = P\{U_{d0}\}$ is a diagonal matrix.

Since $\Delta\theta_{\text{pll}}(s) = \frac{H_{\text{pll}}(s)}{s}\Delta U_q(s)$, substituting its HTF model into (A.3) yields

$$\Delta\boldsymbol{\theta}_{\text{pll}}(s) = \boldsymbol{T}_{\text{pll}}(s)\left[-\boldsymbol{A}_{\sin}(\delta_{\text{pll0}})\ \boldsymbol{A}_{\cos}(\delta_{\text{pll0}})\right]\begin{bmatrix}\Delta\hat{\boldsymbol{U}}_a(s)\\ \Delta\hat{\boldsymbol{U}}_b(s)\end{bmatrix} \tag{A.4}$$

where $\boldsymbol{T}_{\text{pll}}(s)$ contains the frequency-shifted copies of $T_{\text{pll}(0)} = H_{\text{pll}}(s)/(s + U_{d0}H_{\text{pll}}(s))$. Finally, combining (A.2) and (A.5) yields the HTF of the QSG-PLL

$$\Delta\boldsymbol{\theta}_{\text{pll}}(s) = \underbrace{\boldsymbol{T}_{\text{pll}}(s)\left[-\boldsymbol{A}_{\sin}(\delta_{\text{pll0}})\ \boldsymbol{A}_{\cos}(\delta_{\text{pll0}})\right]\begin{bmatrix}\boldsymbol{H}_{\text{sogia}}(s)\\ \boldsymbol{H}_{\text{sogib}}(s)\end{bmatrix}}_{\boldsymbol{G}_{\boldsymbol{\theta}\_u}(s)}\Delta\boldsymbol{U}_a(s) \tag{A.5}$$

2) Modeling of the DC Voltage Control: By linearizing the squared dc voltage, the HTF model of the dc voltage controller is obtained

$$\Delta\boldsymbol{I}_d^{\text{ref}}(s) = 2\boldsymbol{H}_{\text{dc}}(s)\boldsymbol{U}_{\text{dc0}}\cdot\Delta\boldsymbol{U}_{\text{dc}}(s) \tag{A.6}$$

where $\boldsymbol{U}_{\text{dc0}} = P\{U_{\text{dc0}}(t)\}\cdot U_{\text{dc0}}(t)$ is the steady-state dc voltage usually containing even harmonics. $\boldsymbol{H}_{\text{dc}}(s)$ contains the frequency-shifted copies of H_{dc}.

Subsequently, the linearized ac current reference is

$$\Delta i_a^{\text{ref}} = \cos\theta_{\text{pll0}}\Delta i_d^{\text{ref}} - \sin\theta_{\text{pll0}}\Delta i_q^{\text{ref}} - I_{b0}^{\text{ref}}(t)\,\Delta\theta_{\text{pll}} \tag{A.7}$$

where $I_{b0}^{\text{ref}}(t) = \sin\theta_{\text{pll0}}I_{d0}^{\text{ref}}(t) + \cos\theta_{\text{pll0}}I_{q0}^{\text{ref}}(t)$, and $I_{d0}^{\text{ref}}(t)$ and $I_{q0}^{\text{ref}}(t)$ are steady-state *d*-axis and *q*-axis current references, respectively. Since this article assumes a constant reactive current control, thus $\Delta i_q^{\text{ref}} = 0$, so that the HTF model of (A.7) is obtained as

$$\Delta\boldsymbol{I}_a^{\text{ref}} = \boldsymbol{A}_{\cos}(\delta_{\text{pll0}})\Delta\boldsymbol{I}_d^{\text{ref}} - \boldsymbol{I}_{b0}^{\text{ref}}\Delta\boldsymbol{\theta}_{\text{pll}} \tag{A.8}$$

where $\boldsymbol{I}_{b0}^{\text{ref}} = P\{\sin\theta_{\text{pll0}}I_{d0}^{\text{ref}}(t) + \cos\theta_{\text{pll0}}I_{q0}^{\text{ref}}(t)\}$.

Then, combining (A.4), (A.6), and (A.8), the following relation is obtained:

$$\Delta\boldsymbol{I}_a^{\text{ref}}(s) = 2\boldsymbol{A}_{\cos}(\delta_{\text{pll0}})\boldsymbol{H}_{\text{dc}}(s)\boldsymbol{U}_{\text{dc0}}\cdot\Delta\boldsymbol{U}_{\text{dc}}(s) - \boldsymbol{I}_{b0}^{\text{ref}}\boldsymbol{G}_{\theta\_u}(s)\Delta\boldsymbol{U}_a(s) \tag{A.9}$$

3) Modeling of the Current Control: The HTF model of the ac current control is

$$\Delta\boldsymbol{U}_a^{\text{ref}}(s) = \boldsymbol{H}_{\text{PR}}(s)\cdot\left(\Delta\boldsymbol{I}_a^{\text{ref}}(s) - \Delta\boldsymbol{I}_a(s)\right) \tag{A.10}$$

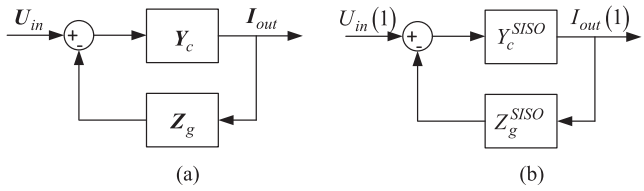

Fig. 12. MIMO- and SISO-equivalent-model-based source and load system.

Then, considering a second-order *Pade* approximation of the control and pulsewidth modulation delay

$$G_{\text{del}}(s) = \frac{1 - \frac{3T_d}{4}s + \frac{T_d^2}{4}s^2}{1 + \frac{3T_d}{4}s + \frac{T_d^2}{4}s^2} \tag{A.11}$$

the HTFs of the CM and DM cases are obtained as

$$\begin{cases}\Delta\boldsymbol{M}_a^{\text{DM}} = \frac{1}{V_{\text{dc}}^{\text{ref}}}G_{\text{del}}(s)\,\Delta U_a^{\text{ref}}(s)\\ \Delta\boldsymbol{M}_a^{\text{CM}} = G_{\text{del}}(s)\,U_{\text{dc0}}^{-1}\left(\Delta U_a^{\text{ref}}(s) - M_0^{\text{ref}}\Delta U_{\text{dc}}(s)\right)\end{cases} \tag{A.12}$$

where $m_{a0}^{\text{ref}}(t)$ is the steady-state modulation index, and $\boldsymbol{M}_0^{\text{ref}} = P\{m_{a0}^{\text{ref}}(t)\}$ is its Toeplitz matrix. $\boldsymbol{G}_{\text{del}}(s)$ contains the frequency-shifted copies of $G_{\text{del}}(s)$.

4) Modeling of the VSC Circuit: According to Fig. 1(a), the linearized state-space model of the main circuit is

$$\frac{d}{dt}\Delta X_c = A_c(t)\,\Delta X_c + B_m(t)\,\Delta m_a^{\text{ref}} + B_u u_a \tag{A.13}$$

where

$$\Delta X_c = \begin{bmatrix}\Delta u_{\text{dc}}\\ \Delta i_a\end{bmatrix},\ A_c(t) = \begin{bmatrix}-\frac{1}{R_L C_{\text{cap}}} & -\frac{m_{a0}^{\text{ref}}(t)}{C_{\text{cap}}}\\ \frac{m_{a0}^{\text{ref}}(t)}{L_f} & -\frac{R_f}{L_f}\end{bmatrix}$$

$$B_m(t) = \left[-\frac{i_{a0}(t)}{C_{\text{cap}}}, \frac{u_{\text{dc0}}(t)}{L_f}\right]^T,\ \text{and}\ B_u = \left[0, -\frac{1}{L_f}\right]^T.$$

Transforming (A.14) into harmonic domain yields

$$(s\boldsymbol{I} + \boldsymbol{N}_{\text{blk}})\,\Delta\boldsymbol{X}_c(s) = \boldsymbol{A}_c\Delta\boldsymbol{X}_c(s) + \boldsymbol{B}_m\Delta\boldsymbol{M}_a^{\text{ref}}(s) + \boldsymbol{B}_u\Delta\boldsymbol{U}_a(s) \tag{A.14}$$

where $\boldsymbol{N}_{\text{blk}} = \text{diag}\,(\cdots, -kj\omega_1\boldsymbol{I}_{2\times2}, \cdots, \boldsymbol{0}_{2\times2}, \cdots, kj\omega_1\boldsymbol{I}_{2\times2}, \cdots)$is a block diagonal matrix; $\boldsymbol{A}_c$,$\boldsymbol{B}_m$, and $\boldsymbol{B}_u$ are the Toeplitz matrices of$A_c(t)$,$B_m(t)$ and $B_u\,\Delta\boldsymbol{X}_c(s) = [\ldots, \Delta X_{c(-1)}, \Delta X_{c(0)}, \Delta X_{c(+1)}, \ldots]^T$; $\Delta\boldsymbol{M}_a^{\text{ref}}(s)$and $\Delta\boldsymbol{U}_a(s)$ are in a format similar to $\Delta\boldsymbol{X}_c(s)$.

Finally, by assembling HTFs (A.8)–(A.12) and (A.14), the VSC harmonic-domain admittance $\boldsymbol{Y}_c^{\text{HTF}}(s)$ is established.

B. Proof of the Identical Stability Conclusion of the SISO Equivalent and MIMO Original System

To achieve a clear comparison in the forthcoming analysis, the detailed models of the grid and VSC are assumed to be 2-by-2 matrices. This will not compromise the generality if higher dimensional matrices are analyzed.

Suppose the grid and VSC model are developed as $\boldsymbol{Z}_g = \begin{bmatrix}Z_{g11} & Z_{g12}\\ Z_{g21} & Z_{g22}\end{bmatrix}$, $\boldsymbol{Y}_c = \begin{bmatrix}Y_{c11} & Y_{c12}\\ Y_{c21} & Y_{c22}\end{bmatrix}$. According to Fig. 12(a), the

closed-loop model for the MIMO system is

$$\boldsymbol{I}_{\text{out}} = (\boldsymbol{I} + \boldsymbol{Y}_c\boldsymbol{Z}_g)^{-1}\boldsymbol{Y}_c\boldsymbol{U}_{ptb} = (\boldsymbol{Z}_c + \boldsymbol{Z}_g)^{-1}U_{ptb} \quad \text{(A.15)}$$

Then, the characteristic equation C_{MIMO} of this MIMO system is obtained from the numerator of $\det(\boldsymbol{Z}_c + \boldsymbol{Z}_g)$, which is

$$C_{\text{MIMO}} = \boldsymbol{\mathcal{N}}\left\{\begin{array}{c}(Z_{g11} + Z_{c11})(Z_{g22} + Z_{c22}) \\ -(Z_{g12} + Z_{c12})(Z_{g21} + Z_{c21})\end{array}\right\} \quad \text{(A.16)}$$

where $\boldsymbol{\mathcal{N}}\{\cdot\}$ is defined as an operator extracting the numerator of an s-domain function.

Furthermore, based on the SISO modeling technique, the VSC and grid-SISO equivalent model evaluated under the first input of U_{in} and the first output I_{out} is derived as follows:

$$\left\{\begin{array}{l} Z_g^{\text{SISO}} = Z_{g11} - Z_{g12}\frac{Z_{c21}+Z_{g21}}{Z_{c22}+Z_{g22}} \\ Z_c^{\text{SISO}} = Z_{c11} - \frac{Z_{c12}(Z_{c21}+Z_{g21})}{Z_{c22}+Z_{g22}}\end{array}\right. \quad \text{(A.17)}$$

The corresponding closed-loop model based on Fig. 12(b) is

$$\begin{aligned} I_{\text{out}}(1) &= \left(1 + Y_c^{\text{SISO}}Z_g^{\text{SISO}}\right)^{-1} \\ Y_c^{\text{SISO}}U_{ptb}(1) &= \left(Z_c^{\text{SISO}} + Z_g^{\text{SISO}}\right)^{-1}U_{ptb}(1) \end{aligned} \quad \text{(A.18)}$$

Then, the characteristic equation C_{SISO} of this SISO equivalent system is obtained as $\boldsymbol{\mathcal{N}}\{Z_c^{\text{SISO}} + Z_g^{\text{SISO}}\}$, which is

$$C_{\text{SISO}} = \boldsymbol{\mathcal{N}}\left\{\frac{(Z_{g11} + Z_{c11})(Z_{c22} + Z_{g22}) - (Z_{c21} + Z_{g21})(Z_{g12} + Z_{c12})}{Z_{c22} + Z_{g22}}\right\} \quad \text{(A.19)}$$

It should be noted that all the components, e.g., Z_{g11}, Z_{c11}, are functions as $Z_{g11} = \frac{N_{g11}(s)}{D_{g11}(s)}$. Since the denominator of $Z_{c22} + Z_{g22}$ also appears in the denominator of $(Z_{g11} + Z_{c11})(Z_{c22} + Z_{g22}) - (Z_{c21} + Z_{g21})(Z_{g12} + Z_{c12})$, therefore they are canceled in (A.19). Based on this, we obtained

$$C_{\text{SISO}} = \boldsymbol{\mathcal{N}}\left\{\begin{array}{c}(Z_{g11} + Z_{c11})(Z_{c22} + Z_{g22}) \\ -(Z_{c21} + Z_{g21})(Z_{g12} + Z_{c12})\end{array}\right\}. \quad \text{(A.20)}$$

By comparing (A.16) and (A.20), we obtain

$$C_{\text{SISO}} = C_{\text{MIMO}} \quad \text{(A.21)}$$

which concludes the proof. This derivation also shows that the SISO impedance modeling technique is applicable to a grid exhibiting frequency coupling behavior.

REFERENCES

[1] R. Teodorescu, M. Liserre, and P. Rodriguez, "Introduction," in *Grid Converters for Photovoltaic Wind Power System*. Chichester, U.K.: Wiley, 2011, pp. 1–4.

[2] N. Flourentzou, V. G. Agelidis, and G D. Demetriades, "VSC-based HVDC power transmission systems: An overview," *IEEE Trans. Power Electron.*, vol. 24, no. 3, pp. 592–602, Mar. 2009.

[3] H. Hu, Y. Shao, L. Tang, J. Ma, Z. He, and S. Gao, "Overview of harmonic and resonance in railway electrification systems," *IEEE Trans. Ind. Appl.*, vol. 54, no. 5, pp. 5227–5245, Sep./Oct. 2018.

[4] H. Liu*et al.* "Subsynchronous interaction between direct-drive PMSG based wind farms and weak AC networks," *IEEE Trans. Power Syst.*, vol. 32, no. 6, pp. 4708–4720, Nov. 2017.

[5] C. Li, "Unstable operation of photovoltaic inverter from field experiences," *IEEE Trans. Power Del.*, vol. 33, no. 2, pp. 1013–1015, Apr. 2018.

[6] J. Sun, "Impedance-based stability criterion for grid-connected inverters," *IEEE Trans. Power Electron.*, vol. 26, no. 11, pp. 3075–3078, Nov. 2011.

[7] X. Wang and F. Blaabjerg, "Harmonic stability in power electronic-based power systems: Concept, modeling, and analysis," *IEEE Trans. Smart Grid*, vol. 10, no. 3, pp. 2858–2870, May 2019.

[8] L. Harnefors, "Modeling of three-phase dynamic systems using complex transfer functions and transfer matrices," *IEEE Trans. Ind. Electron.*, vol. 54, no. 4, pp. 2239–2248, Aug. 2007.

[9] M. Belkhayat, "Stability criteria for AC power systems with regulated loads," Ph.D. dissertation, Purdue Univ., West Lafayette, IN, USA, 1997.

[10] B. Wen, D. Boroyevich, R. Burgos, P. Mattavelli, and Z. Shen, "Small-signal stability analysis of three-phase AC systems in the presence of constant power loads based on measured d-q frame impedances," *IEEE Trans. Power Electron.*, vol. 30, no. 10, pp. 5952–5963, Oct. 2015.

[11] L. Harnefors, M. Bongiorno, and S. Lundberg, "Input-admittance calculation and shaping for controlled voltage-source converters," *IEEE Trans. Ind. Electron.*, vol. 54, no. 6, pp. 3323–3334, Dec. 2007.

[12] A. Gelb and W. E. V. Velde, *Multiple-Input Describing Functions and Nonlinear System Design*, New York, NY, USA:McGraw-Hill, 1968.

[13] A. Lesnicar and R. Marquardt, "An innovative modular multilevel converter topology suitable for a wide power range," in *Proc. IEEE PowerTech Conf.*, Bologna, Italy, vol. 3, p. 6, Jun. 23–26, 2003, doi: 10.1109/PTC.2003.1304403.

[14] H. Zhang, Z. Liu, S. Wu, and Z. Li, "Input impedance modeling and verification of single-phase voltage source converters based on harmonic linearization," *IEEE Trans. Power Electron.*, vol. 34, no. 9, pp. 8544–8554, Sep. 2019.

[15] M. Cespedes and J. Sun, "Impedance modeling and analysis of grid-connected voltage-source converters," *IEEE Trans. Power Electron.*, vol. 29, no. 3, pp. 1254–1261, Mar. 2014.

[16] J. Sun and H. Liu, "Sequence impedance modeling of modular multilevel converters," *IEEE J. Emerg. Sel. Topics Power Electron.*, vol. 5, no. 4, pp. 1427–1443, Dec. 2017.

[17] X. Wang, L. Harnefors, F. Blaabjerg, and P.C. Loh, "A unified impedance model of voltage-source converters with phase-locked loop effect," in *Proc. IEEE Energy Convers. Congr. Expo.*, 2016, pp. 1–8.

[18] A. Rygg, M. Molinas, C. Zhang, and X. Cai, "A modified sequence-domain impedance definition and its equivalence to the dq-domain impedance definition for the stability analysis of AC power electronic systems," *IEEE J. Emerg. Sel. Topics Power Electron.*, vol. 4, no. 4, pp. 1383–1396, Dec. 2016

[19] M. Kazem Bakhshizadeh *et al.*, "Couplings in phase domain impedance modeling of grid-connected converters," *IEEE Trans. Power Electron.*, vol. 31, no. 10, pp. 6792–6796, Oct. 2016.

[20] N. M. Wereley, "Analysis and control of linear periodically time varying systems," Ph.D. thesis, Dept. Aeronaut. Astronaut., Massachusetts Inst. Technol., cambridge, MA, USA, 1990.

[21] P. Vanassche, G. Gielen, and W. M. Sansen, *Systematic Modeling and Analysis of Telecom Frontends and their Building Blocks*. New York, NY, USA: Springer, 2006.

[22] J. Kwon, X. Wang, F. Blaabjerg, C. L. Bak, V. Sularea, and C. Busca, "Harmonic interaction analysis in a grid-connected converter using harmonic state-space (HSS) modeling," *IEEE Trans. Power Electron.*, vol. 32, no. 9, pp. 6823–6835, Sep. 2017.

[23] J. Kwon, X. Wang, C. L. Bak, and F. Blaabjerg, "Harmonic instability analysis of single-phase grid connected converter using harmonic state space (HSS) modeling method," in *Proc. IEEE Energy Convers. Congr. Expo.*, Montreal, QC, Canada, 2015, pp. 2421–2428.

[24] J. Lyu, X. Zhang, X. Cai, and M. Molinas, "Harmonic state-space based small-signal impedance modeling of a modular multilevel converter with consideration of internal harmonic dynamics," *IEEE Trans. Power Electron.*, vol. 34, no. 3, pp. 2134–2148, Mar. 2019.

[25] H. Wu, X. Wang, and Ł. Kocewiak, "Impedance-based stability analysis of voltage-controlled MMCs feeding linear AC systems," *IEEE J. Emerg. Sel. Topics Power Electron.*, p. 1, Apr. 2019, doi: 10.1109/JESTPE.2019.2911654.

[26] H. Wang, M. Wu, and J. Sun, "Analysis of low-frequency oscillation in electric railways based on small-signal modeling of vehicle-grid system in dq frame," *IEEE Trans. Power Electron.*, vol. 30, no. 9, pp. 5318–5330, Sep. 2015.

[27] Y. Liao, Z. Liu, H. Zhang, and B. Wen, "Low-frequency stability analysis of single-phase system withdq-frame impedance approach—Part I: Impedance modeling and verification," *IEEE Trans. Ind. Appl.*, vol. 54, no. 5, pp. 4999–5011, Sep./Oct. 2018.
[28] S. Lissandron, L. D. Santa, P. Mattavelli, and B. Wen, "Experimental validation for impedance-based small-signal stability analysis of single-phase interconnected power systems with grid-feeding inverters," *IEEE J. Emerg. Sel. Topics Power Electron.*, vol. 4, no. 1, pp. 103–115, Mar. 2016.
[29] S. Shah and L. Parsa, "On impedance modeling of single-phase voltage source converters," in *Proc. IEEE Energy Convers. Congr. Expo.*, Milwaukee, WI, USA, 2016, pp. 1–8.
[30] Q. Qian, S. Xie, J. Xu, K. Xu, S. Bian, and N. Zhong, "Output impedance modeling of single-phase grid-tied inverters with capturing the frequency-coupling effect of PLL," *IEEE Trans. Power Electron.*, p. 1, Oct. 2019, doi: 10.1109/TPEL.2019.2946984
[31] J A. Antonopoulos, L. Angquist, and H. Nee, "On dynamics and voltage control of the modular multilevel converter," in *Proc. 13th Eur. Conf. Power Electron. Appl.*, Barcelona, Spain, 2009, pp. 1–10.
[32] V. Salis, A. Costabeber, S. M. Cox, and P. Zanchetta, "Stability assessment of power-converter-based AC systems by LTP theory: Eigenvalue analysis and harmonic impedance estimation," *IEEE J. Emerg. Sel. Topics Power Electron.*, vol. 5, no. 4, pp. 1513–1525, Dec. 2017.
[33] C. Zhang, X. Cai, A. Rygg, and M. Molinas, "Sequence domain SISO equivalent models of a grid-tied voltage source converter system for small-signal stability analysis," *IEEE Trans. Energy Convers.*, vol. 33, no. 2, pp. 741–749, Jun. 2018.

Chen Zhang received the B.Eng. degree from the China University of Mining and Technology, China, in 2011, and the Ph.D. degree from Shanghai Jiao Tong University, China, in 2018.

In 2015, he was a Visiting Ph.D. Scholar with the Department of Engineering Cybernetics, Norwegian University of Science and Technology (NTNU), Norway. He is currently a Postdoctoral Research Fellow with NTNU. His research interests include modeling and stability analysis of voltage-source converter (VSC)-based energy conversion systems, where the aim is to reveal the fundamental dynamics and stability mechanisms of renewable energies with VSCs as the grid interface.

Marta Molinas (Member, IEEE) received the Diploma in electromechanical engineering from the National University of Asuncion, Asuncion, Paraguay, in 1992; the M.Eng. degree from Ryukyu University, Japan, in 1997; and the Doctor of Engineering degree from the Tokyo Institute of Technology, Tokyo, Japan, in 2000.

She was a Guest Researcher with the University of Padova, Padova, Italy, in 1998. From 2004 to 2007, she was a Postdoctoral Researcher with the Norwegian University of Science and Technology (NTNU), where she was a Professor with the Department of Electric Power Engineering from 2008 to 2014. She is currently a Professor with the Department of Engineering Cybernetics, NTNU. Her research interests include stability of power electronics systems, harmonics, instantaneous frequency, and nonstationary signals from the human and the machine.

Dr. Molinas is an Editor for the IEEE JOURNAL OF EMERGING AND SELECTED TOPICS IN POWER ELECTRONICS and the IEEE TRANSACTIONS ON ENERGY CONVERSION. She is also an Associate Editor for the IEEE TRANSACTIONS ON POWER ELECTRONICS. She was an AdCom Member of the IEEE Power Electronics Society from 2009 to 2011.

Sjur Føyen (Member, IEEE) received the master's degree in electric power engineering from the Norwegian University of Science and Technology, Trondheim, Norway, in 2018. He is currently working toward the doctoral degree with the Department of Electric Power Engineering, NTNU.

His research interests include synchronization, time–frequency analysis, and stability of power electronics systems.

Jon Are Suul (Member, IEEE) received the M.Sc. degree in energy and environmental engineering and the Ph.D. degree in electric power engineering from the Norwegian University of Science and Technology (NTNU), Trondheim, Norway, in 2006 and 2012, respectively.

From 2006, he was with SINTEF Energy Research, Trondheim, Norway, where he was engaged in simulation of power electronic converters and marine propulsion systems until starting his PhD studies. Since 2012, he has been working as a part-time Research Scientist at SINTEF Energy Research, and has also been a Postdoctoral Researcher with the Department of Electric Power Engineering of NTNU until 2016. Since August 2017, he has been an Adjunct Associate Professor with the Department of Engineering Cybernetic, NTNU. His research interests include modeling, analysis, and control of power electronic converters in HVdc transmission systems, renewable energy applications, and electrification of transport.

Dr. Suul is an Associate Editor for the IEEE JOURNAL OF EMERGING AND SELECTED TOPICS IN POWER ELECTRONICS.

Takanori Isobe (Member, IEEE) was born in Hamamatsu, Japan, in 1978. He received the B.Eng. degree in physical electronics, the M.Eng. degree in nuclear engineering, and the D.Eng. degree in energy sciences from the Tokyo Institute of Technology, Tokyo, Japan, in 2003, 2005, and 2008, respectively.

From 2008 to 2010 and from 2012 to 2013, he was a Researcher with the Tokyo Institute of Technology, where he was an Assistant Professor from 2010 to 2012. From 2013 to 2014, he was with MERSTech, Tokyo. In 2013, he joined the University of Tsukuba, Tsukuba, Japan, where he is currently an Associate Professor with the Faculty of Pure and Applied Sciences. His research interests include static reactive power compensators and soft-switching power converters.

Dr. Isobe is a member of the Institute of Electrical Engineers of Japan and the Japan Institute of Power Electronics.